University of Nebraska - Lincoln
DigitalCommons@University of Nebraska - Lincoln

Alexei Gruverman Publications | Research Papers in Physics and Astronomy

2017

Theoretical Approach to Electroresistance in Ferroelectric Tunnel Junctions

Sou-Chi Chang
Georgia Institute of Technology

Azad Naeemi
Georgia Institute of Technology

Dmitri E. Nikonov
Intel Corporation, Hillsboro, Oregon

Alexei Gruverman
University of Nebraska - Lincoln, agruverman2@unl.edu

Follow this and additional works at: http://digitalcommons.unl.edu/physicsgruverman

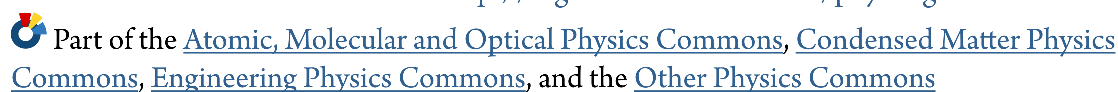
Part of the Atomic, Molecular and Optical Physics Commons, Condensed Matter Physics Commons, Engineering Physics Commons, and the Other Physics Commons

Chang, Sou-Chi; Naeemi, Azad; Nikonov, Dmitri E.; and Gruverman, Alexei, "Theoretical Approach to Electroresistance in Ferroelectric Tunnel Junctions" (2017). *Alexei Gruverman Publications*. 66.
http://digitalcommons.unl.edu/physicsgruverman/66

This Article is brought to you for free and open access by the Research Papers in Physics and Astronomy at DigitalCommons@University of Nebraska - Lincoln. It has been accepted for inclusion in Alexei Gruverman Publications by an authorized administrator of DigitalCommons@University of Nebraska - Lincoln.

Theoretical Approach to Electroresistance in Ferroelectric Tunnel Junctions

Sou-Chi Chang* and Azad Naeemi
School of Electrical and Computer Engineering, Georgia Institute of Technology, Atlanta, Georgia 30332, USA

Dmitri E. Nikonov
Components Research, Intel Corporation, Hillsboro, Oregon 97124, USA

Alexei Gruverman
Department of Physics and Astronomy, University of Nebraska, Lincoln, Nebraska 68588, USA
(Received 21 July 2016; revised manuscript received 2 December 2016; published 6 February 2017)

In this paper, a theoretical approach comprising the nonequilibrium Green's function method for electronic transport and the Landau-Khalatnikov equation for electric polarization dynamics is presented to describe polarization-dependent tunneling electroresistance (TER) in ferroelectric tunnel junctions. Using appropriate contact, interface, and ferroelectric parameters, the measured current-voltage characteristic curves in both inorganic ($Co/BaTiO_3/La_{0.67}Sr_{0.33}MnO_3$) and organic (Au/PVDF/W) ferroelectric tunnel junctions can be well described by the proposed approach. Furthermore, under this theoretical framework, the controversy of opposite TER signs observed experimentally by different groups in $Co/BaTiO_3/La_{0.67}Sr_{0.33}MnO_3$ systems is addressed by considering the interface termination effects using the effective contact ratio defined through the effective screening length and dielectric response at the metal-ferroelectric interfaces. Finally, our approach is extended to investigate the role of a CoO_x buffer layer at the $Co/BaTiO_3$ interface in a ferroelectric tunnel memristor. It is shown that in order to have a significant memristor behavior not only the interface oxygen vacancies but also the CoO_x layer thickness may vary with the applied bias.

DOI: 10.1103/PhysRevApplied.7.024005

I. INTRODUCTION

Over the past four decades, the computing performance has been exponentially improved in a microchip because of doubled device density occurring approximately every two years according to Moore's law [1]. However, at the same time, as the complementary metal-oxide-semiconductor (CMOS) technology is downscaled to the nanometer regime, the static power consumption plays a nontrivial role in total power dissipation due to a significant amount of leakage currents in memory and logic devices [2]. As a consequence, recently, active research has also been under way in pursuit of low-power and nonvolatile memory and logic circuits in the beyond-CMOS technologies [3]. The major advantages of the nonvolatility in the microprocessor potentially are (i) the system speed improvement by eliminating the need of transferring data between volatile power-starving memories (i.e., static and dynamic random-access memories) and external nonvolatile storage (i.e., hard disk drive) as well as (ii) the energy-efficiency enhancement by removing the static power consumption.

Among many emerging nonvolatile memory technologies, ferroelectric (FE) devices based on quantum-mechanical tunneling known as ferroelectric tunnel junctions (FTJs) have attracted significant attention due to the extremely high on:off ratio, very low write power, and nondestructive read [4]. The concept of a FTJ has been demonstrated experimentally [5–9] thanks to improved technologies in fabricating high-quality ultrathin FE films by pulsed laser deposition or off-axis sputtering, which push the critical thickness of ferroelectricity down to a few unit cells [10–14]. Moreover, over the past decade, FE fabrication technologies have become mature and compatible to the back-end CMOS process [15], and, therefore, FTJ CMOS circuits with additional microchip functionality may become a reality in the near future.

In a FTJ, the switching of resistance, also known as the tunneling electroresistance (TER) effect, is achieved by the polarization reversal in the FE barrier via applied voltage. The TER effect is fundamentally different from other resistive switching mechanisms such as the formation of conductive filaments within a metal-oxide insulator in an atomic switch [16], the oxygen-vacancy-assisted conduction in a resistive random-access memory [17], and the magnetization-dependent tunneling in a magnetic tunnel junction (MTJ) [18]. In particular, unlike tunneling magnetoresistance (TMR) in the MTJ, which is typically only a few hundred percent [19–21], TER in a FTJ can easily reach $10^5\%$ [8], offering a much more reliable *read*

*souchi@gatech.edu

 © 2017 American Physical Society

mechanism for the stored memory bits. While significant TER is achieved in FTJs, there still exists a controversy in TER signs, particularly for $Co/BaTiO_3/La_{0.67}Sr_{0.33}MnO_3$ (Co/BTO/LSMO) systems [7,22]; that is, TER signs observed experimentally from different groups are completely opposite. Note that the term "TER sign" is introduced here to specify the relation between the electric polarization direction and the resistance state. The TER sign is defined as "+" (positive) and "−" (negative) when the low (*on*) resistance state is produced by the polarization pointing to the top and the bottom electrodes, respectively. Recent experimental work shows that these opposite TER signs can be attributed to the dead layers induced by either TiO_2 or BaO termination at the Co/BTO interface [23].

In addition to the promising progress in the FTJ experiments, many theoretical efforts have also been made in predicting or understanding TER in a FTJ. Inspired by the polar switch concept proposed Esaki *et al.* [24] in 1971, the giant TER was predicted near the zero bias based on electron direct tunneling [25,26]. Using a similar model, enhanced TER by inserting a nonpolar dielectric layer at the metal-FE interface was also predicted near the equilibrium [27]. Furthermore, going beyond the equilibrium, polarization-dependent TER was predicted to be based either solely on direct tunneling [28] or on a combination of several transport mechanisms including direct tunneling, Fowler-Nordheim tunneling, and thermionic emission [29]. Nevertheless, works on polarization-dependent TER were mainly based on the analytical models derived from the Wenzel-Kramer-Brillouin approximation and did not include a realistic FE hysteresis loop. More important, most of the theoretical approaches describe the experimental data in the low-voltage range; so far, none of them have provided quantitative comparisons with current-voltage (*I-V*) characteristics measured from a full FE hysteresis sweep, which is extremely important in designing FTJs as memory elements, where both *read* and *write* operations need to be well described. This paper presents a comprehensive approach to (i) describe the experimentally measured *I-V* relations for various types of FTJs and (ii) to explain the discrepancy in the TER signs observed experimentally by different groups in the Co/BTO/LSMO-layered structures. The developed approach includes the nonequilibrium Green's function (NEGF) method for electronic transport under different bias conditions [30] and the thermodynamics-based Landau-Khalatnikov equation for a complete ferroelectric hysteresis loop.

A FTJ structure is shown in Fig. 1(a), where the device is composed of a FE thin film sandwiched between two metallic electrodes. In this work, TER is assumed to be induced by band-structure modifications through the electrostatic effect due to polarization reversal (Fig. 3). Moreover, to explore the role of a CoO_x buffer layer in the Co/BTO/LSMO systems reported to be an inevitable byproduct while depositing the metallic electrode [22], a FTJ structure with a nonpolar dielectric (DE) layer at the metal-FE interface is also considered as shown in Fig. 1(b).

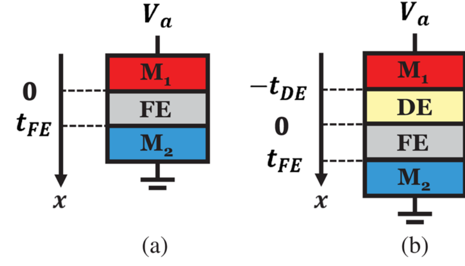

FIG. 1. Schematics of FTJs in the (a) absence and (b) presence of a nonpolar DE layer between the FE and metallic electrode. M_1 and M_2 are top and bottom metallic electrodes, respectively.

The rest of this paper is organized as follows. In Sec. II, mathematical details of the proposed approach for TER in a FTJ is presented. In Sec. III, using this theoretical model, good agreement with the experimental *I-V* characteristics is shown for various FTJs, and the discrepancy in the reported TER sign in Co/BTO/LSMO systems is explained by introducing the termination effect using the effective contact ratios. Also, the model is extended to investigate the role of a CoO_x buffer layer in a FE memristor. Section IV concludes the paper.

II. THEORETICAL FORMALISM

A. FTJ without nonpolar dielectric

To describe the polarization-dependent TER in a FTJ, the energy band diagram under the effects of the applied electric field, built-in field, and depolarization field is considered. In this work, the applied electric field is generated by a bias voltage across a FTJ, the built-in field is mainly due to the work function difference between layered materials [31–33], and the depolarization field is induced by the incomplete screening of the FE bound charge. Figures 2(a)–2(c) illustrate electrostatic potential profiles induced by the applied electric field, built-in field, and depolarization field for FTJs in the presence and absence of a nonpolar DE layer, respectively. Mathematically, for a FTJ without a nonpolar DE layer, we assume that the potential profiles within metals (V_{M1} and V_{M2}) follow the Thomas-Fermi expression [34] and are given as (see Appendix A for detailed derivations)

$$V_{M1}(x) = \frac{-\rho_s \lambda_1}{\epsilon_1 \epsilon_0} e^{(x/\lambda_1)}, \tag{1}$$

$$V_{M2}(x) = \frac{\rho_s \lambda_2}{\epsilon_2 \epsilon_0} e^{[-(x-t_{\mathrm{FE}})/\lambda_2]}, \tag{2}$$

where ρ_s is the screening charge density at the FE-metal interfaces (C/m^2), λ_1 and λ_2 are the effective screening lengths of the top and bottom FE-metal interfaces,

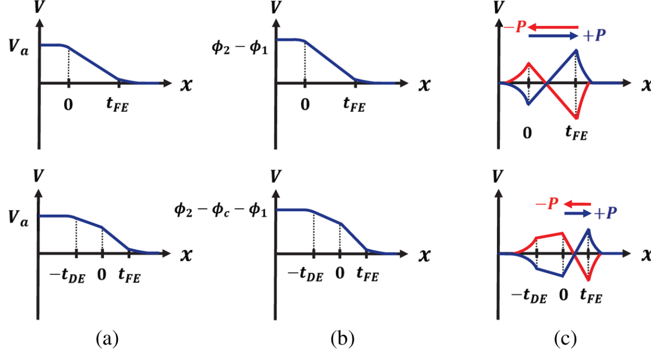

FIG. 2. Schematics of electrostatic potential profiles due to (a) applied electric field, (b) built-in field, and (c) depolarization field for FTJs with (bottom panel) and without (top panel) a nonpolar DE layer between the FE and top metallic electrode.

respectively, ϵ_1 and ϵ_2 are relative dielectric constants of the top and bottom FE-metal interfaces, respectively, and ϵ_0 is the vacuum dielectric constant. Note that the imperfect screening here is described by both the effective screening length and dielectric constant rather than the Thomas-Fermi one since it is generally accepted that the imperfect screening is determined not only by the metal but also by the FE thin film and the specific interface geometry [35]. As a result, from Eqs. (1) and (2), the potential drop in the top and bottom electrodes is $[\rho_s\lambda_1/(\epsilon_1\epsilon_0)]$ and $[\rho_s\lambda_2/(\epsilon_2\epsilon_0)]$, respectively. As described in Eq. (3), in a FTJ, by applying Gauss's law near the metal-FE interface, the electrical displacement in the FE is equal to the free charge density at the FE-metal interface,

$$\rho_s = \epsilon_0 E_{\mathrm{FE}} + P, \tag{3}$$

where P is the electric polarization of the FE, and E_{FE} is the total electric field across the FE. Furthermore, due to the fact that the potential drop induced by the applied bias and built-in field has to be completely shared by both metallic electrodes and the FE, the following equation is satisfied,

$$\frac{\rho_s\lambda_1}{\epsilon_1\epsilon_0} + \frac{\rho_s\lambda_2}{\epsilon_2\epsilon_0} + E_{\mathrm{FE}}t_{\mathrm{FE}} = V_a + V_{\mathrm{BI}}, \tag{4}$$

where V_a is the applied voltage and V_{BI} is the voltage drop due to the built-in field defined as $[(\phi_2 - \phi_1 - E_{F2} + E_{F1})/e]$ with ϕ_1 and ϕ_2 being conduction-band discontinuities at the top and bottom FE-metal interfaces, respectively, E_{F1} and E_{F2} being Fermi energies of the top and bottom metallic electrodes, respectively, and e being the elementary charge. From Eqs. (3) and (4), the total electric field across the FE is given as

$$E_{\mathrm{FE}} = \frac{V_a + V_{\mathrm{BI}} - P\left(\frac{\lambda_1}{\epsilon_1\epsilon_0} + \frac{\lambda_2}{\epsilon_2\epsilon_0}\right)}{t_{\mathrm{FE}} + \frac{\lambda_1}{\epsilon_1} + \frac{\lambda_2}{\epsilon_2}}. \tag{5}$$

Note that the depolarization field E_{dep} is obtained by canceling the built-in field with the applied bias ($V_a + V_{\mathrm{BI}} = 0$) and given as

$$E_{\mathrm{dep}} = \frac{-P\left(\frac{\lambda_1}{\epsilon_1\epsilon_0} + \frac{\lambda_2}{\epsilon_2\epsilon_0}\right)}{t_{\mathrm{FE}} + \frac{\lambda_1}{\epsilon_1} + \frac{\lambda_2}{\epsilon_2}}. \tag{6}$$

By replacing E_{FE} in Eq. (3) with Eq. (6), the screening charge density induced simply by the FE bound charge $\rho_{s,p}$ is given as

$$\rho_{s,p} = \frac{P}{1 + \frac{\lambda_1}{t_{\mathrm{FE}}\epsilon_1} + \frac{\lambda_2}{t_{\mathrm{FE}}\epsilon_2}}, \tag{7}$$

which is consistent with the common expression shown in Ref. [26].

The energy band diagram is constructed by assuming that the bulk properties of metallic electrodes remain the same under the applied bias; that is, the Fermi energy of the metal is fixed. Illustrated in Fig. 3(a) by setting the conduction-band edge in the top metallic contact as the zero-energy reference, chemical potentials at the top and bottom contacts (μ_1 and μ_2, respectively) have to satisfy the following equation:

$$\begin{aligned} eV_a &= \mu_2 - \mu_1 \\ &= \left(\frac{\rho_s\lambda_1}{\epsilon_1\epsilon_0} + \phi_1 + E_{\mathrm{FE}}t_{\mathrm{FE}} - \phi_2 + \frac{\rho_s\lambda_2}{\epsilon_2\epsilon_0} + E_{F2}\right) - E_{F1}. \end{aligned} \tag{8}$$

B. FTJ with nonpolar dielectric

When a nonpolar DE layer is present between the top electrode and the FE layer [(Fig. 1(b)], a procedure similar to the one presented in Sec. II A can be used to obtain the electric fields and potential profiles in a FTJ. Again, by applying Gauss's law near the metal-FE interface and also assuming that the electric displacement is continuous at the DE-FE interfaces, as well as assuming the net voltage drop has to be entirely shared within the device, the following equations are satisfied

$$\rho_s = \epsilon_0 E_{\mathrm{FE}} + P = \epsilon_0\epsilon_{\mathrm{DE}}E_{\mathrm{DE}}, \tag{9}$$

$$V_a + V_{\mathrm{BI}} = \frac{\rho_s\lambda_1}{\epsilon_1\epsilon_0} + \frac{\rho_s\lambda_2}{\epsilon_2\epsilon_0} + E_{\mathrm{FE}}t_{\mathrm{FE}} + E_{\mathrm{DE}}t_{\mathrm{DE}}, \tag{10}$$

where E_{DE} is the electric field across the DE, and ϵ_{DE} is the dielectric constant of the nonpolar layer. By solving Eqs. (9) and (10), the interface screening charge density and electric fields across the FE and the nonpolar DE are given as

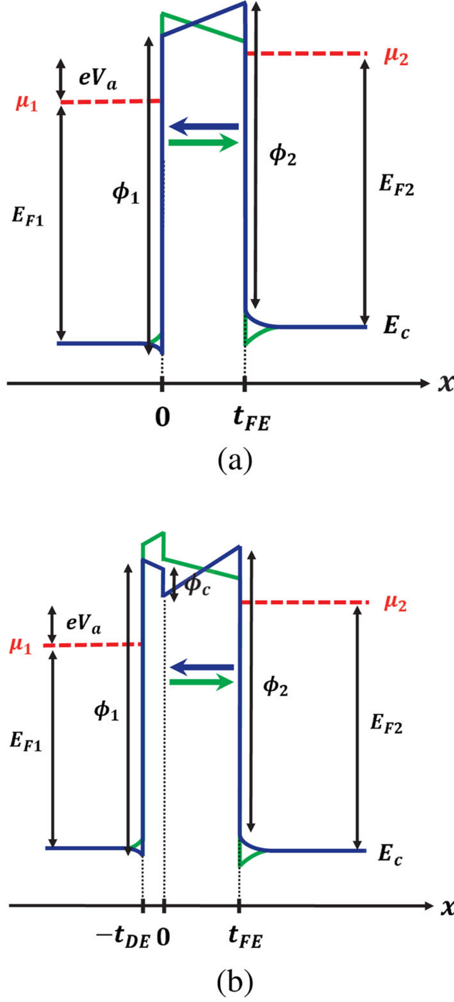

FIG. 3. Energy band diagrams at a bias voltage V_a satisfying $\mu_2 - \mu_1 = eV_a$ for FTJs (a) without and (b) with a nonpolar DE layer between the FE and metallic electrode. Arrows in the FE represent the direction of the electric polarization.

$$\rho_s = \frac{\frac{\epsilon_0}{t_{\mathrm{FE}}}(V_a + V_{\mathrm{BI}}) + P}{1 + \frac{t_{\mathrm{DE}}}{\epsilon_{\mathrm{DE}} t_{\mathrm{FE}}} + \frac{\lambda_1}{\epsilon_1 t_{\mathrm{FE}}} + \frac{\lambda_2}{\epsilon_2 t_{\mathrm{FE}}}}, \tag{11}$$

$$E_{\mathrm{FE}} = \frac{\rho_s - P}{\epsilon_0}, \tag{12}$$

$$E_{\mathrm{DE}} = \frac{\rho_s}{\epsilon_{\mathrm{DE}} \epsilon_0}, \tag{13}$$

where V_{BI} now is defined as $[(\phi_2 + \phi_c - \phi_1 - E_{F2} + E_{F1})/e]$ with ϕ_c being the band discontinuity at the FE-nonpolar DE interface. Note that the screening charge density induced solely by the FE bound charge can be obtained by removing both V_a and V_{BI} in Eq. (11), and the resulting expression is consistent with that in Ref. [27]. After knowing the incomplete screening charge at the interface, the corresponding depolarization field can be calculated using Eq. (12) and is given as

$$E_{\mathrm{dep}} = \frac{-P\left(\frac{t_{\mathrm{DE}}}{\epsilon_{\mathrm{DE}}} + \frac{\lambda_1}{\epsilon_1} + \frac{\lambda_2}{\epsilon_2}\right)}{\epsilon_0\left(t_{\mathrm{FE}} + \frac{t_{\mathrm{DE}}}{\epsilon_{\mathrm{DE}}} + \frac{\lambda_1}{\epsilon_1} + \frac{\lambda_2}{\epsilon_2}\right)}. \tag{14}$$

As expected, Eq. (14) reduces to Eq. (6) when t_{DE} reduces to zero. Similarly, by using the same energy reference in the previous case, the FTJ energy band diagram with a nonpolar DE layer, as shown in Fig. 3(b), is established by satisfying the following equation:

$$\begin{aligned} eV_a &= \mu_2 - \mu_1 \\ &= \left(\frac{\rho_s \lambda_1}{\epsilon_1 \epsilon_0} + \phi_1 + E_{\mathrm{DE}} t_{\mathrm{DE}} - \phi_c + E_{\mathrm{FE}} t_{\mathrm{FE}} \right. \\ &\quad \left. - \phi_2 + \frac{\rho_s \lambda_2}{\epsilon_2 \epsilon_0} + E_{F2}\right) - E_{F1}. \end{aligned} \tag{15}$$

C. FE hysteresis loop

To describe the electric polarization response of a FE thin film under applied bias, built-in field, and depolarization field, the Landau-Khalatnikov (LK) equation is used and given as [36]

$$\gamma \frac{\partial P}{\partial t} = -\frac{\partial F}{\partial P}, \tag{16}$$

where γ is the viscosity coefficient, and F is the FE free energy including the bulk and interactions with different types of electric fields, which can be, in general, expanded in terms of the thermodynamic order parameter based on the Landau theory and is written as

$$F = \alpha_1 P^2 + \alpha_{11} P^4 + \alpha_{111} P^6 - E_a P - E_{\mathrm{BI}} P - \frac{1}{2} E_{\mathrm{dep}} P, \tag{17}$$

where α_1, α_{11}, and α_{111} are the free-energy expansion coefficients [33,37–39], E_a is the applied electric field, and E_{BI} is the built-in field. In Eq. (17), the first three terms are for the bulk FE free energy, the contributions from the applied electric and built-in fields are described by the fourth and fifth terms, respectively, and the last term represents the self-energy of the depolarization field (thus, the factor of $\frac{1}{2}$) [38].

While Ref. [37] pointed out that Eq. (16) is mainly applicable to the intrinsic single-domain FE switching, which typically requires a defect-free FE thin film with a very small cross-sectional area and is quite different from the extrinsic switching driven by FE domain nucleation and propagation, here for simplicity, we assume that the electric polarization in a FE thin film can be represented by an effective electric polarization P satisfying the LK equation. Additionally, the experimental FE hysteresis loops characterized by the remanent polarization and coercive voltage

can be well described by adjusting the expansion and viscosity coefficients. Furthermore, by using Eq. (16), the shift in a FE hysteresis loop due to a nonzero built-in field across a FTJ can also be easily captured [33]. Note that the electric displacement through the FE, D, is written as [40]

$$D = \epsilon_0(1+\chi)E_{\mathrm{FE}} + P_d, \tag{18}$$

where χ accounts for the linear contribution of the polarization, and P_d is the polarization due to switching dipoles. However, in the LK equation mentioned above, P accounts for the effects from both linear response and switching dipoles, and, thus, the electric displacement is simply written as $\epsilon_0 E_{\mathrm{FE}} + P$.

D. Tunneling currents

As shown in Fig. 3, based on Eqs. (8) and (15), the energy band diagram can be constructed for a given electric polarization obtained from the LK equation and is used as the electron potential energy in the NEGF method to calculate the transmission coefficient [30]. For the tunneling currents, the Landau formula is applied and given as [41]

$$J = -\sum_{k_y,k_z} \frac{2e}{Ah} \int dE t(E)\{f_1(E) - f_2(E)\}, \tag{19}$$

where k_y and k_z are electron wave vectors in the transverse plane, e is the elementary charge, A is the cross-sectional area, E is the total electron energy, and t is the transmission coefficient. f_1 and f_2 are Fermi-Dirac distributions for the top and bottom metallic contacts, respectively, given as

$$f_{1(2)}(E) = \frac{1}{1+e^{[E-\mu_{1(2)}/(k_B T)]}}, \tag{20}$$

where μ_1 and μ_2 are chemical potentials of the top and bottom metallic contacts with $\mu_2 - \mu_1 = eV_a$, k_B is the Boltzmann constant, and T is the temperature. The details of writing an alternative expression for currents using the electron wave vector in the spherical coordinates are given in Appendix B. The transmission coefficient in Eq. (19) is calculated using the Green's function $\mathbf{G}$ given as

$$t = \mathrm{trace}(\mathbf{\Gamma^t G \Gamma^b G^\dagger}), \tag{21}$$

where $\mathbf{G}$ is defined as $(E\mathbf{I} - \mathbf{H} - \Sigma_\mathbf{t} - \Sigma_\mathbf{b})^{-1}$ with $\mathbf{I}$, $\mathbf{H}$, and Σ being the identity matrix, device Hamiltonian, and contact self-energy, respectively, and $\mathbf{\Gamma}$ is the broadening function defined as $i(\Sigma - \Sigma^\dagger)$. The detailed expression of the Hamiltonian and contact self-energy can be found in the Appendix C.

III. RESULTS AND DISCUSSION

In this section, the theoretical framework presented above is used to explain existing experimental results [7,9,22]. First, to show that the model captures key underlying physics behind FTJs, the measured I-V characteristics for both inorganic and organic FTJs are fitted by using the proper energy band diagram and LK parameters. Next, the concept of effective screening length and dielectric constant is applied to explain the opposite high- and low-resistance states observed in Co/BTO/LSMO systems [7,22], which may result from interface termination effects [23]. Finally, the model is extended by including a CoO_x nonpolar buffer layer at the Co/BTO interface, and it is shown that the voltage-dependent oxygen vacancies at the CoO_x/BTO interface may be partially responsible for the memristor behavior as mentioned in Ref. [22].

A. Comparison with experimental I-V characteristics

In this paper, for a FTJ, it is assumed that TER is a main consequence of modifying the energy band diagram through depolarization fields induced by incomplete screening charge at FE-metal interfaces, and it is expected to vary with the polarization. In other words, at a given voltage, a larger difference in two opposite polarization states leads to more pronounced TER. Hence, to describe the measured FTJ I-V characteristics, it is required to accurately model FE hysteresis loops, which are also presented in the following comparisons with experiments. Note that for simplicity, all of the FE hysteresis loops in this work are simulated by applying a sinusoidal voltage signal with a period of 70 ps, and the LK parameters are adjusted accordingly to obtain a reasonable FE response observed in the experiments. In reality, FE thin films may have different dynamic responses with respect to an applied bias, depending on the quality, material, or size of the sample.

First, the measured FTJ I-V characteristics in a Co/BTO/LSMO layered structure [7] are used to justify our theoretical approach. Since there is no clear shift in hysteresis loops observed in the experiments, it is assumed that a built-in field across the junction is close to zero, which implies ϕ_1 is equal to ϕ_2 in our model. Next, the LK parameters for BTO [34] are slightly varied so that the FE thin film exhibits a hysteresis loop with $V_c \sim \pm 3$ V, $\epsilon_{\mathrm{FE}} \sim 11$, and $P_r \sim 0.3$ C/m^2 as shown in Fig. 4(b), where V_c, ϵ_{FE}, and P_r are the coercive voltage, the FE dielectric constant, and the remanent polarization, respectively. By assuming the following interface parameters: $\lambda_1 = 0.5 \times 10^{-10}$ m [42], and $\lambda_2 = 1 \times 10^{-10}$ m [42], ϕ_1, ϵ_1, ϵ_2, and m^* are varied to obtain a good agreement with experimental data, while ϕ_2 is assumed to be equal to ϕ_1 as shown in Fig. 4(a), which shows that in Co/BTO/LSMO systems, a depolarization field modifying the energy band diagram

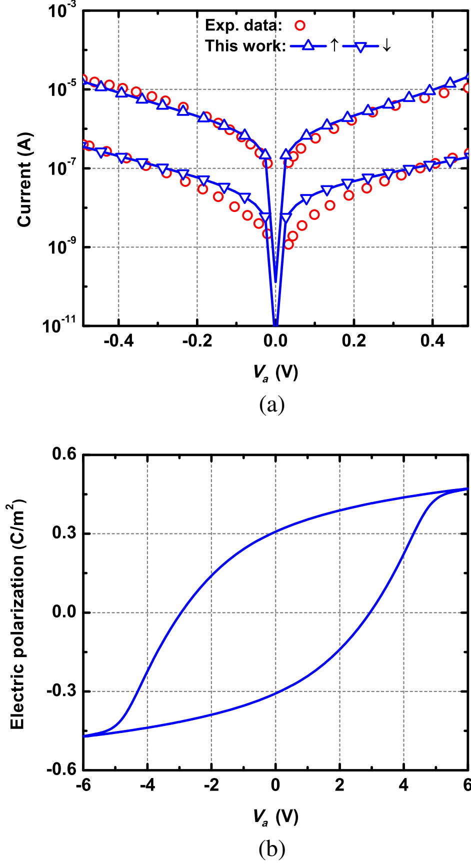

FIG. 4. (a) Comparison between FTJ (Co/BTO/LSMO) experimental data (diameter $= 700$ nm) [7] and simulation results using the following band diagram parameters: $t_{\mathrm{FE}} = 2$ nm, $\phi_1 = \phi_2 = 7.15$ eV, $E_{F1} = E_{F2} = 6.5$ eV, $\epsilon_1 = 2.4$, $\epsilon_2 = 9.6$, $\lambda_1 = 0.5 \times 10^{-10}$ m [42], $\lambda_2 = 1 \times 10^{-10}$ m [42], $m^* = 0.8 m_0$. (b) Simulated FE hysteresis loop for FTJ (Co/BTO/LSMO) experiments [7] ($V_c \sim \pm 3$ V, $\epsilon_{\mathrm{FE}} \sim 11$, and $P_r \sim 0.3$ C/m^2) with the following LK parameters: $\gamma = 1.8 \times 10^{-2}$ msec/F, $\alpha_1 = -2.77 \times 10^7$ m/F, $\alpha_{11} = -5.35 \times 10^8$ m^5/C^{2}F, and $\alpha_{111} = 2 \times 10^{10}$ m^9/C^{4}F.

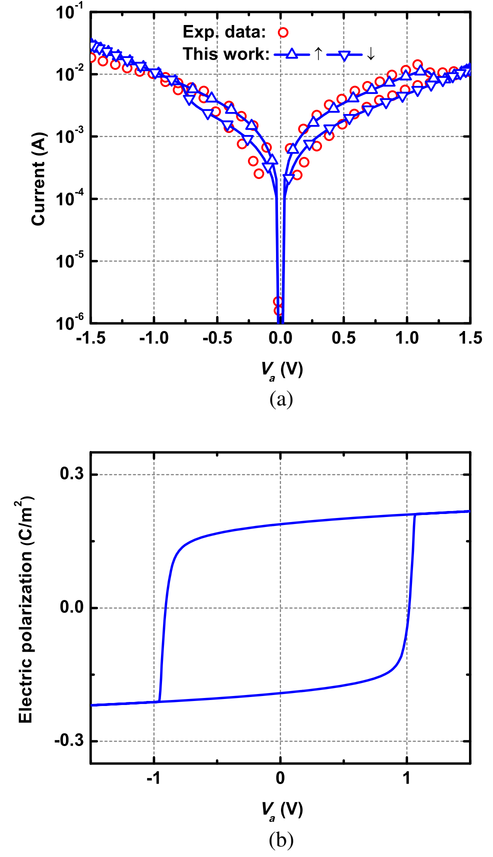

FIG. 5. (a) Comparison between FTJ (Au/PVDF/W) experimental data [9] and simulation results using the following band diagram parameters: $t_{\mathrm{FE}} = 2$ nm, $\phi_1 = 6.76$ eV, $\phi_2 = 6.7$ eV, $E_{F1} = E_{F2} = 6.5$ eV, $\epsilon_1 = 6.5$, $\epsilon_2 = 20$, $\lambda_1 = 0.75 \times 10^{-10}$ m [45], $\lambda_2 = 0.45 \times 10^{-10}$ m [46], $m^* = 0.1 m_0$. (b) Simulated FE hysteresis loop for FTJ (Au/PVDF/W) experiments [9] ($V_c \sim \pm 1$ V, $\epsilon_{\mathrm{FE}} \sim 4.4$, and $P_r \sim 0.18$ C/m^2) with the following LK parameters: $\gamma = 1.5 \times 10^{-3}$ m sec/F, $\alpha_1 = -1.38 \times 10^9$ m/F, $\alpha_{11} = -2.67 \times 10^{10}$ m^5/C^{2}F, and $\alpha_{111} = 8 \times 10^{11}$ m^9/C^{4}F.

is the dominant driving force for TER rather than the effects due to strain [28] or FE-polarization-dependent complex band structure [43]. However, even though the experimental data can be well described by depolarization fields in Fig. 4, the change in the FTJ energy band diagrams through polarization reversals is not a purely charge-mediated (or electrostatic) effect. This is mainly because the effective screening length and the dielectric response significantly depend on the specific interface geometry, which is a fully quantum-mechanical outcome and requires approaches in the microscopic level such as first-principles calculations [44].

In Fig. 4, since only the currents at low voltages are measured, the full dependence of the tunneling currents on a FE hysteresis loop cannot be observed. As a result, an *I-V* characteristic curve reported in an Au/polyvinylidene fluoride (PVDF)/W-layered structure is used to justify our model for a complete FE sweep [9]. Again, to fit experimental data, a FE hysteresis loop of a monolayer PVDF film is generated by tuning the LK parameters as shown in Fig. 5(b), in which the resulting V_c, ϵ_{FE}, and P_r are about 1 V, 4.4, and 0.18 C/m^2, respectively. By using the following interface parameters: $\epsilon_1 = 6.5$, $\lambda_1 = 0.75 \times 10^{-10}$ m [45], and $\lambda_2 = 0.45 \times 10^{-10}$ [46], ϕ_1, ϕ_2, ϵ_2, and m^* are adjusted to match experimental data as shown in Fig. 5(a), where a good agreement between the theoretical and experimental results is reached. Note that a weak built-in field observed in the experiment [9] leading to a small shift in the hysteresis loop as shown in Fig. 5(b) is included to obtain a better fit to the experimental data.

In Fig. 5(a), it can be seen that TER varies largely with the electric polarization; that is, the difference between the high- and low-resistance states is reduced as the voltage is close to or beyond the coercive voltage. Furthermore, since the interface parameters for Fig. 5(a) are closer to bulk values, it can also be concluded that TER in an

Au/PVDF/W organic FTJ is dominated more by a pure electrostatic effect rather than complex changes of interfacial bonds, which can be attributed to the fact that the electrodes are attached to PVDF thin films using mainly van der Waals forces in an Au/PVDF/W structure [9].

B. Interface termination effects on TER

As shown in Figs. 4 and 5, in both experiments [7,9], the low- and high-resistance states correspond to the electric polarizations pointing to the top (Co or Au) and the bottom (LSMO or W) electrodes, respectively. These experimental results can be explained by the energy band diagram shown Fig. 6(a), where a lower tunnel barrier is produced as the polarization points to the top contact, which has larger changes in the interface potential energy. Note that as shown in Eqs. (1) and (2), a higher ratio of λ/ϵ leads to a larger change in the interface potential energy. From Fig. 6(a), we find that since at low voltages, the energy slope on the FE barrier is mostly dominated by the depolarization field, whose direction is always opposite to that of the polarization, the top and bottom interfaces have opposite effects on the tunnel barrier. Using the polarization pointing to the top contact as an example, the top and bottom interface potential changes reduce and increase the FE barrier, respectively, and these contact effects on the barrier are reversed as the polarization is switched to the opposite direction. Consequently, if the interface energy change at the top is greater than that at the bottom, the FE barrier for the polarization pointing to the top will be lower, and, thus, a lower resistance state is generated. Therefore, as shown in Fig. 6(a), it seems that interface quantities play a significant role in determining the relation between the high- and low-resistance states and the polarization direction. Here, a quantity called the effective contact ratio is defined as $[\lambda_1\epsilon_2/(\lambda_2\epsilon_1)]$ to distinguish the high- and low-resistance states in a FTJ. In Figs. 4 and 5, the effective contact ratios are 1.96 and 5.1, respectively, which are both larger than 1, implying that the resistance states are more dominated by the top interface. As a result, the lower-resistance state is for the polarization pointing to the top contact (or the TER sign is +), consistent with experimental observations.

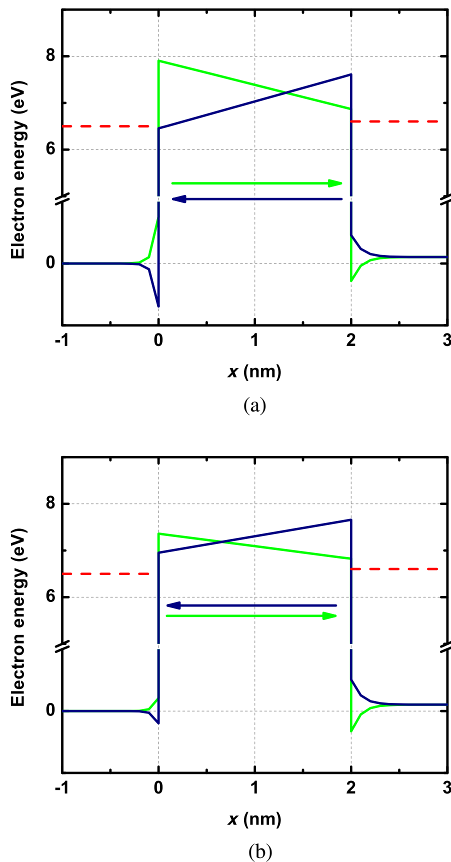

FIG. 6. Energy band diagrams at 0.1 V for both polarization states with two different effective contact ratios: (a) 1.98 and (b) 0.49. The dark blue and the green correspond to the polarization states pointing to the top and bottom contacts, respectively. Red dashed lines represent chemical potentials at both contacts.

In Au/PVDF/W FTJs, it is believed that a depolarization field creates larger changes in the potential energy at the Au side [9], and so far, no experimental evidence shows that high- or low-resistance states can be switched in the same FTJ structure, which is probably because contacts and an organic FE film are attached through van der Waals forces rather than the complex interface bonds as mentioned previously [9]. However, in Co/BTO/LSMO-layered structures, several groups have reported an opposite relation between the polarization direction and the resistance state [7,22]. Recently, some groups have reported that the reversal of the high- and low-resistance states in Co/BTO/LSMO systems is attributed to either TiO_2 or BaO terminated at the Co/BTO interface [23]. To support this argument theoretically, our model provides an intuitive picture for the reversal of high- and low-resistance states induced by termination effects. As predicted by first-principles calculations, the screening length is almost zero at the Pt/BaO-terminated BTO interface [44]. From Ref. [23], it has also been shown that the interface termination effects on the TER signs in FTJs using Pt and Co as the top electrodes are consistent. Therefore, here we assume that similar to the Pt/BaO interface, the effective screening length at the Co/BaO-terminated BTO interface is much less than that at the Co/TiO_2 BTO interface. In Fig. 6(b), the effective contact ratio is set to be less than 1 without adjusting λ/ϵ of the bottom interface. It is shown that compared to Fig. 6(a), where the effective contact ratio is larger than 1, a lower tunneling barrier is generated by the polarization pointing to the bottom electrode rather than the top one, and, thus, the high- and low-resistance states are reversed.

Figures 7(a) and 7(b) clearly indicate that rather than the individual interface properties, the effective contact ratio is the most essential factor to determine both the sign and

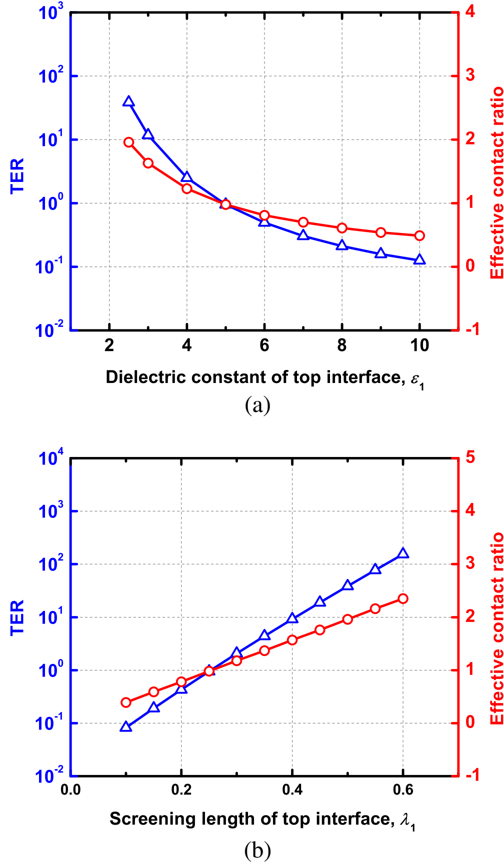

FIG. 7. TER at $V_a = 0.1$ V and effective contact ratio versus top contact (a) dielectric constant and (b) screening length. TER and effective contact ratios are defined as $I_\uparrow/I_\downarrow$ and $[\lambda_1\epsilon_2/(\lambda_2\epsilon_1)]$, respectively.

magnitude of TER defined as $I_\uparrow/I_\downarrow$, where $I_\uparrow$ and $I_\downarrow$ are the currents corresponding to the polarizations pointing to the top and bottom electrodes, respectively. In Figs. 7(a) and 7(b), it is shown that a more pronounced TER can be produced as the top and the bottom interfaces become more distinct ($[\lambda_1\epsilon_2/(\lambda_2\epsilon_1)] \gg 1$ or $\ll 1$). Also, from the same figures, a lower resistance state is always produced by the polarization pointing to the interface with larger λ/ϵ as explained in Figs. 6(a) and 6(b). In other words, the sign of TER, as it is defined here, is switched from + to − as the effective contact ratio changes from the value larger than 1 to less than 1. As a result, if the effective contact ratio is equal to 1, meaning that the device is perfectly symmetric, the resulting TER will also be 1, and, thus, it is impossible to distinguish the polarization direction through tunneling resistance.

C. FTJs with CoO_x

From the previous section, it is shown that TER significantly depends on metal-BTO interface properties in a FTJ. Moreover, in addition to the termination effect, recently some experimental studies have reported that an inevitable CoO_x layer at the Co/BTO interface plays an important role in the memristive, i.e., tunable resistance, behavior of a Co/BTO/LSMO FTJ; that is, reading TER varies with the magnitude of the previous writing voltage [22]. Hence, in this section, our simple model is extended as shown in Figs. 1(b) and 3(b) to investigate the CoO_x effect on TER.

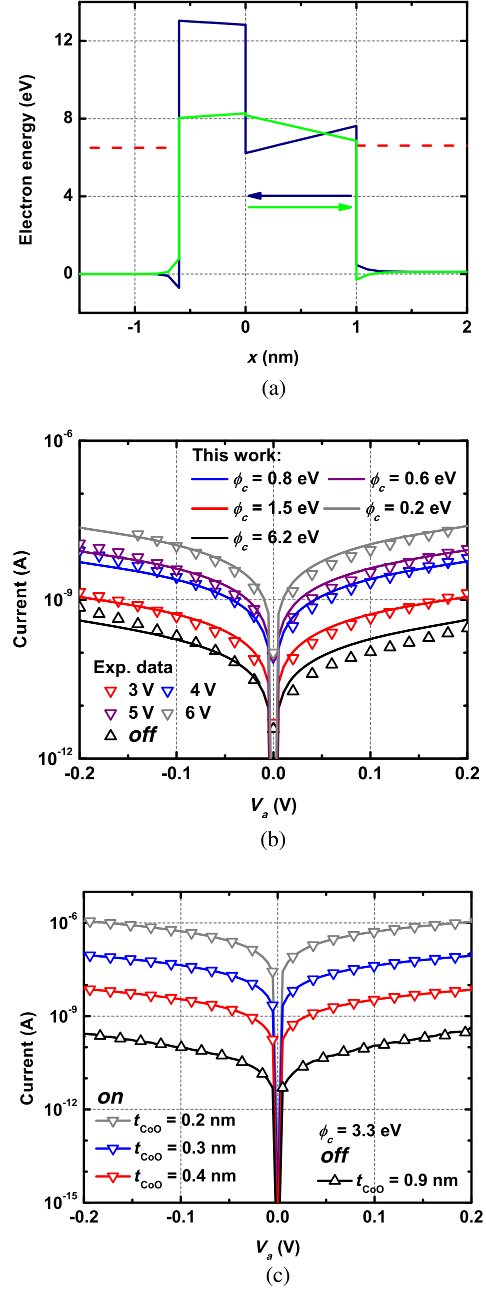

FIG. 8. (a) Energy band diagrams at 0.1 V for high- and low-resistance states in a FTJ with a CoO_x buffer layer at the interface. ϕ_c for high- and low-resistance states are 6.6 and 0.1 eV, respectively. (b) Comparison with experimental data [22] using various ϕ_c for high- and low-resistance states and different writing voltages. In addition to $t_{DE} = 0.6$ nm, $t_{FE} = 1$ nm, ϕ_1, and ϕ_c, the simulation parameters are the same as those in Fig. 4. (c) Tunneling current versus applied voltage under different CoO_x thicknesses with ϕ_c being 3.3 eV.

As mentioned in Ref. [22], a positive (negative) applied bias accumulates (dissipates) oxygen vacancies at the CoO_x/BTO interface, effectively reducing (increasing) ϕ_c. Therefore, as shown in the energy band diagrams of Fig. 8(a), which are constructed using Eq. (15), the low- (high-) resistance state corresponds to the polarization pointing to the bottom (top) contact with smaller (larger) ϕ_c. Note that as predicted in Ref. [27], an unchanged ϕ_c in both polarization directions results in a reversal of the high- and low-resistance states, which are not observed in the experiment yet [22]. Furthermore, since no significant shift in the FE hysteresis loop is observed in the experiment [22], in our model, ϕ_1 is adjusted accordingly with ϕ_c so that the built-in field across the device is zero. In other words, $\phi_2 + \phi_c - \phi_1 = 0$, where ϕ_2 is fixed due to no change at the BTO/LSMO interface. Therefore, by using the same simulation parameters for the interfaces and the FE hysteresis loop as listed in Fig. 4, and assuming that part of BTO transforms into CoO_x ($t_{DE} = 0.6$ nm and $t_{FE} = 1$ nm), ϕ_c is adjusted to fit the experimental data as shown in Fig. 8(b), where a good agreement between the theory and the experiment is reached. As a result, Fig. 8(b) shows that it is possible to change TER through modifications of ϕ_c induced by voltage-dependent oxygen vacancies at the CoO_x/BTO interface. However, it seems that the required change in ϕ_c from *off* to *on* states may be too drastic for simply the charge-mediated effect (6.6 to 0.1 eV). Therefore, the thickness of CoO_x may also be altered depending on the applied bias; that is, the CoO_x thickness may be reduced (increased) as the FTJ is switched from high- (low-) to low- (high-) resistance states, and, thus, TER is varied with the CoO_x thickness as shown in Fig. 8(c). More experimental studies are required to confirm the possibility of the voltage-dependent CoO_x thickness in a FTJ.

IV. CONCLUSION

This paper presents a theoretical description of quantum-mechanical electronic transport and thermodynamic ferroelectric responses in both organic and inorganic FTJs. The inverse TER effect with respect to the polarization direction reported by different groups can also be explained by the proposed model through the effective contact ratio and termination effects. Finally, the role of a CoO_x buffer layer at the Co/BTO interface is also examined. We find that the sizable memristive effects, i.e., tunable resistance, cannot be explained solely by the change in the barrier height due to charge-mediated effects. It is suggested that the CoO_x layer thickness may also change as a result of electrically induced Co oxidation or reduction at the Co/BTO interface. The proposed approach for description of the electroresistance effect in FTJs provides a foundation for performance optimization of the core elements for nonvolatile memory and logic devices.

ACKNOWLEDGMENTS

The authors acknowledge support by the Benchmarking Center and the Center for Nanoferroic Devices (CNFD), Semiconductor Research Corporation Nanoelectronics Research Initiative (SRC-NRI) under Task No. 2624.001 and No. 2398.002, sponsored by NIST and the Nanoelectronics Research Corporation (NERC). A. G. also acknowledges support by the National Science Foundation under Grant No. ECCS-1509874.

APPENDIX A: DERIVATION OF EQS. (2) AND (3)

The relation between charge (Q) and electric field (E) in the metal can be described by Poisson's equation given as

$$\frac{\partial E(x)}{\partial x} = \frac{Q}{\epsilon_m \epsilon_0} = \frac{-e(n - n_0)}{\epsilon_m \epsilon_0}, \tag{A1}$$

where ϵ_m is the dielectric constant of the metal, n is the electron density, and n_0 is the electron density in the neutral metallic electrode. In the metal, the electrons can be treated as a free Fermi gas, and, thus, the local potential (V) and electron density can be related as [47]

$$V = \frac{\hbar^2}{2m_0}(3\pi^2 n)^{\frac{2}{3}}, \tag{A2}$$

with $\hbar$ being the reduced Planck constant, and m_0 being the free-electron mass. By using $-[(\partial V)/\partial x] = E$, the derivative of the electron density with respect to x can be expressed as

$$\frac{\partial n}{\partial x} = -\frac{E}{\frac{\hbar^2}{3m_0}(3\pi^2)^{\frac{2}{3}} n^{\frac{-1}{3}}}, \tag{A3}$$

and, therefore, the derivative of Eq. (A1) with respect to x becomes

$$\frac{\partial^2 E}{\partial x^2} = \frac{-e}{\epsilon_m \epsilon_0}\frac{\partial n}{\partial x} = \frac{E}{\lambda^2}, \tag{A4}$$

where the metal Thomas-Fermi screening length λ is defined as $[\hbar^2 \epsilon_m \epsilon_0/(3em_0)](3\pi^2)^{\frac{2}{3}} n^{\frac{-1}{3}}$. The general solution of Eq. (A4) is $Ae^{(x/\lambda)} + Be^{(-x/\lambda)}$ with A and B being coefficients determined by the boundary conditions, which are, using the top electrode as an example, $E(-\infty) = 0$ and $E(0) = [\rho_s/(\epsilon_1 \epsilon_0)]$. Therefore, the corresponding electric field (E_1) and potential profile (V_1) ($-\infty < x \leq 0$) are given as

$$E_1 = \frac{\rho_s}{\epsilon_1 \epsilon_0} e^{(x/\lambda_1)}, \tag{A5}$$

$$V_1 = -\int_{-\infty}^{x} dx' E(x') = \frac{-\rho_s \lambda_1}{\epsilon_1 \epsilon_0} e^{(x/\lambda_1)}. \tag{A6}$$

Similarly, by using $E(\infty)=0$ and $E(t_{\rm FE})=[-\rho_s/(\epsilon_2\epsilon_0)]$ as boundary conditions, the potential profile (V_2) of the bottom electrode ($t_{\rm FE}\le x<\infty$) is given as

$$V_2=\frac{\rho_s\lambda_2}{\epsilon_2\epsilon_0}e^{[-(x-t_{\rm FE})/\lambda_2]}. \tag{A7}$$

Equations (A6) and (A7) are identical to Eqs. (1) and (2). Note that as mentioned in the main text, for some FTJs with complex interfacial bonds, the potential drop near the interface is described by the effective screening length and dielectric response rather than the Thomas-Fermi one [35].

APPENDIX B: ALTERNATIVE EXPRESSION OF EQ. (19)

The electron wave vector can be represented in the spherical coordinate as shown in Fig. 9. To rewrite Eq. (19), the first step is to convert the summation into the integral using periodic boundary conditions ($\sum_k=(L/2\pi)\int dk$), and the resulting expression is given as

$$J=\frac{-e}{2\pi^2 h}\int_{-\infty}^{\infty}\int_{-\infty}^{\infty}dk_y dk_z\int dEt(f_1-f_2). \tag{B1}$$

Note that t, f_1, and f_2 are all energy dependent. Under the spherical coordinate, $dk_y dk_z$ can be written as $k^2\sin\theta d\phi d\theta$. For electrons coming from $+x$ with total energy E equal to $E=[(\hbar^2k^2)/2m^*]+U_0$, where m^* is the effective mass and U_0 is the potential energy, the current equation becomes

$$\begin{aligned}J&=\frac{-e}{2\pi^2 h}\int_0^{2\pi}\int_0^{\frac{\pi}{2}}d\phi d\theta k^2\sin\theta\int dEt(f_1-f_2)\\&=\frac{-em}{\pi^2\hbar^3}\int_0^{\frac{\pi}{2}}d\theta\sin\theta\int_{U_0}^{\infty}dE(E-U_0)t(f_1-f_2).\end{aligned} \tag{B2}$$

It can be seen from Eq. (B2) that the tunneling currents account for all the contribution of electrons from different energy levels and injection angles in the metallic contact.

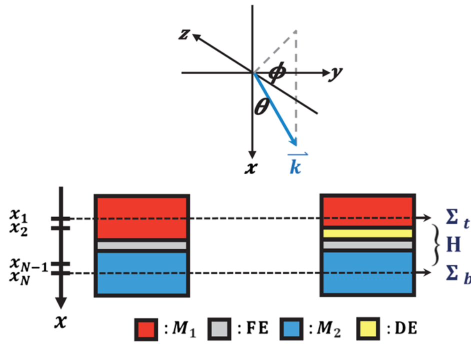

FIG. 9. Schematics illustrating the electron wave vector in the spherical coordinate and the NEGF approach to FTJs without and with a nonpolar DE layer between the FE and metallic electrode.

APPENDIX C: DEVICE HAMILTONIAN AND CONTACT SELF-ENERGY

The device Hamiltonian $\mathbf{H}$ is constructed based on a single-band effective mass Hamiltonian operator of an electron given as

$$\hat{H}=\frac{-\hbar^2}{2m^*}\frac{\partial^2}{\partial x^2}+\frac{\hbar^2(k_y^2+k_z^2)}{2m^*}+U(x), \tag{C1}$$

where $U(x)$ is the energy band diagram of a FTJ. Note that in this approach, a space-independent effective mass m^* is used to characterize the quantum-mechanical tunneling process in the thin-film device. Therefore, by considering an electron coming from $+x$ with total energy E equal to $E=[(\hbar^2k^2)/2m^*]+U_0$, the operator can be rewritten using Fig. 9 and is given as

$$\begin{aligned}\hat{H}&=\frac{-\hbar^2}{2m^*}\frac{\partial^2}{\partial x^2}+(E-U_0)\sin^2\theta+U(x)\\&=\frac{-\hbar^2}{2m^*}\frac{\partial^2}{\partial x^2}+E_\perp(\theta)+U(x),\end{aligned} \tag{C2}$$

where $E_\perp$ is the transverse energy of the electron, which depends on the injection angle, θ. The device Hamiltonian can be obtained by simply converting $\hat{H}$ into a matrix using the finite-difference method and is given as

$$\mathbf{H}=\begin{bmatrix}2t+E_\perp(\theta)+U(x_1) & -t & 0 & \cdots & \cdots & 0 & 0 & 0\\ -t & 2t+E_\perp(\theta)+U(x_2) & -t & 0 & \cdots & \cdots & 0 & 0\\ \vdots & \vdots & \ddots & \ddots & \ddots & \ddots & \vdots & \vdots\\ 0 & 0 & \cdots & \cdots & 0 & -t & 2t+E_\perp(\theta)+U(x_{N-1}) & -t\\ 0 & 0 & 0 & \cdots & \cdots & 0 & -t & 2t+E_\perp(\theta)+U(x_N)\end{bmatrix}, \tag{C3}$$

where the x axis is divided into N mesh points, $x_1,x_2,\ldots,x_{N-1}$, and x_N, and t is the coupling strength between the nearest neighbors defined as $t=[\hbar^2/(2m^*a^2)]$ with a being the distance between two nearest mesh points, which is set as 0.1 nm in the main text. Under the open-boundary condition, the self-energies of the top and bottom contacts are given as

$$\Sigma_{\mathbf{t}} = \begin{bmatrix} -te^{ik_{x,t}a} & 0 & \cdots \\ 0 & 0 & \\ \vdots & & \ddots \end{bmatrix},$$

$$\Sigma_{\mathbf{b}} = \begin{bmatrix} \ddots & & \vdots \\ & 0 & 0 \\ \cdots & 0 & -te^{ik_{x,b}a} \end{bmatrix}, \tag{C4}$$

where $k_{x,t}$ and $k_{x,b}$ are longitudinal electron wave vectors inside the top and bottom electrodes, respectively, given as

$$k_{x,t} = \frac{\cos^{-1}\{1 - \frac{E-U(x_1)-E_{\perp}(\theta)}{2t}\}}{a}, \tag{C5}$$

$$k_{x,b} = \frac{\cos^{-1}\{1 - \frac{E-U(x_N)-E_{\perp}(\theta)}{2t}\}}{a}. \tag{C6}$$

In addition to TER in FTJs, the same approach can also be applied to other problems such as spin injection from a ferromagnet into a semiconductor or a metal [48,49], as long as the energy band diagram is known.

[1] G. E. Moore, Cramming more components onto integrated circuits, in *Proceedings of the IEEE* (IEEE, 1998), Vol. 86, pp. 82–85.

[2] N. S. Kim, T. Austin, D. Baauw, T. Mudge, K. Flautner, J. S. Hu, M. J. Irwin, M. Kandemir, and V. Narayanan, Leakage current: Moore's law meets static power, Computer **36**, 68 (2003).

[3] D. E. Nikonov and I. A. Young, Benchmarking of beyond-CMOS exploratory devices for logic integrated circuits, IEEE J. Explor. Solid-State Comput. Devices Circuits **1**, 3 (2015).

[4] Adrian M. Ionescu, Nanoelectronics: Ferroelectric devices show potential, Nat. Nanotechnol. **7**, 83 (2012).

[5] A. Gruverman, D. Wu, H. Lu, Y. Wang, H. W. Jang, C. M. Folkman, M. Ye. Zhuravlev, D. Felker, M. Rzchowski, C.-B. Eom, and E. Y. Tsymbal, Tunneling electroresistance effect in ferroelectric tunnel junctions at the nanoscale, Nano Lett. **9**, 3539 (2009).

[6] J. Rodriguez Contreras, H. Kohlstedt, U. Poppe, R. Waser, C. Buchal, and N. A. Pertsev, Resistive switching in metal-ferroelectricmetal junctions, Appl. Phys. Lett. **83**, 4595 (2003).

[7] Andre Chanthbouala, Arnaud Crassous, Vincent Garcia, Karim Bouzehouane, Stephane Fusil, Xavier Moya, Julie Allibe, Bruno Dlubak, Julie Grollier, Stephane Xavier, Cyrile Deranlot, Amir Moshar, Roger Proksch, Neil D. Mathur, Manuel Bibes, and Agnes Barthelemy, Solid-state memories based on ferroelectric tunnel junctions, Nat. Nanotechnol. **7**, 101 (2012).

[8] Vincent Garcia and Manuel Bibes, Ferroelectric tunnel junctions for information storage and processing, Nat. Commun. **5**, 4289 (2014).

[9] B. B. Tian, J. L. Wang, S. Fusil, Y. Liu, X. L. Zhao, S. Sun, H. Shen, T. Lin, J. L. Sun, C. G. Duan, M. Bibes, A. Barthelemy, B. Dkhil, V. Garcia, X. J. Meng, and J. H. Chu, Tunnel electroresistance through organic ferroelectrics, Nat. Commun. **7**, 11502 (2016).

[10] V. Nagarajan, S. Prasertchoung, T. Zhao, H. Zheng, J. Ouyang, R. Ramesh, W. Tian, X. Q. Pan, D. M. Kim, C. B. Eom, H. Kohlstedt, and R. Waser, Size effects in ultrathin epitaxial ferroelectric heterostructures, Appl. Phys. Lett. **84**, 5225 (2004).

[11] Y. S. Kim, D. H. Kim, J. D. Kim, Y. J. Chang, T. W. Noh, J. H. Kong, K. Char, Y. D. Park, S. D. Bu, J.-G. Yoon, and J.-S. Chung, Critical thickness of ultrathin ferroelectric $BaTiO_3$ films, Appl. Phys. Lett. **86**, 102907 (2005).

[12] S. K. Streiffer, J. A. Eastman, D. D. Fong, Carol Thompson, A. Munkholm, M. V. Ramana Murty, O. Auciello, G. R. Bai, and G. B. Stephenson, Observation of Nanoscale 180° Dependence Stripe Domains in Ferroelectric $PbTtiO_3$ Thin Films, Phys. Rev. Lett. **89**, 067601 (2002).

[13] Dillon D. Fong, G. Brian Stephenson, Stephen K. Streiffer, Jeffrey A. Eastman, Orlando Auciello, Paul H. Fuoss, and Carol Thompson, Ferroelectricity in ultrathin perovskite films, Science **304**, 1650 (2004).

[14] Na Sai, Alexie M. Kolpak, and Andrew M. Rappe, Ferroelectricity in ultra-thin perovskite films, Phys. Rev. B **72**, 020101 (2005).

[15] H. Toyoshima, S. Kobayashi, J. Yamada, T. Miwa, H. Koike, H. Takeuchi, H. Mori, N. Kasai, Y. Maejima, N. Tanabe, T. Tatsumi, and H. Hada, Feram device and circuit technologies fully compatible with advanced CMOS, in *Proceedings of IEEE Conference on Custom Integrated Circuits*, 2001, pp. 171–178, http://ieeexplore.ieee.org/document/929749/.

[16] Masakazu Aono and Tsuyoshi Hasegawa, The atomic switch, Proc. IEEE **98**, 2228 (2010).

[17] H. Akinaga and H. Shima, Resistive random access memory (RERAM) based on metal oxides, Proc. IEEE **98**, 2237 (2010).

[18] S. Tehrani, Jon M. Slaughter, M. DeHerrera, B. N. Engel, N. D. Rizzo, J. Salter, M. Durlam, R. W. Dave, J. Janesky, B. Butcher, K. Smith, and G. Grynkewich, Magnetoresistive random access memory using magnetic tunnel junctions, Proc. IEEE **91**, 703 (2003).

[19] Shinji Yuasa, Taro Nagahama, Akio Fukushima, Yoshishige Suzuki, and Koji Ando, Giant room-temperature magnetoresistance in single-crystal Fe/MgO/Fe magnetic tunnel junctions, Nat. Mater. **3**, 868 (2004).

[20] Stuart S. P. Parkin, Christian Kaiser, Alex Panchula, Philip M. Rice, Brian Hughes, Mahesh Samant, and See-Hun Yang, Giant tunnelling magnetoresistance at room temperature with MgO (100) tunnel barriers, Nat. Mater. **3**, 862 (2004).

[21] S. Ikeda, J. Hayakawa, Y. Ashizawa, Y. M. Lee, K. Miura, H. Hasegawa, M. Tsunoda, F. Matsukura, and H. Ohno, Tunnel magnetoresistance of 604% at 300 K by suppression of Ta diffusion in CoFeB-MgO-CoFeB pseudo-spin-valves annealed at high temperature, Appl. Phys. Lett. **93**, 082508 (2008).

[22] D. J. Kim, H. Lu, S. Ryu, C.-W. Bark, C.-B. Eom, E. Y. Tsymbal, and A. Gruverman, Ferroelectric tunnel memristor, Nano Lett. **12**, 5697 (2012).

[23] Hiroyuki Yamada, Atsushi Tsurumaki-Fukuchi, Masaki Kobayashi, Takuro Nagai, Yoshikiyo Toyosaki, Hiroshi

Kumigashira, and Akihito Sawa, Strong surface-termination effect on electroresistance in ferroelectric tunnel junctions, Adv. Funct. Mater. **25**, 2708 (2015).
[24] L. Esaki, R. B. Laibowitz, and P. J. Stiles, IBM Technical Disclosure Bulletin **13**, 2161 (1971).
[25] Evgeny Y. Tsymbal and Hermann Kohlstedt, Tunneling across a ferroelectric, Science **313**, 181 (2006).
[26] M. Ye. Zhuravlev, R. F. Sabirianov, S. S. Jaswal, and E. Y. Tsymbal, Giant Electroresistance in Ferroelectric Tunnel Junctions, Phys. Rev. Lett. **94**, 246802 (2005).
[27] M. Ye. Zhuravlev, Y. Wang, S. Maekawa, and E. Y. Tsymbal, Tunneling electroresistance in ferroelectric tunnel junctions with a composite barrier, Appl. Phys. Lett. **95**, 052902 (2009).
[28] H. Kohlstedt, N. A. Pertsev, J. Rodríguez Contreras, and R. Waser, Theoretical current-voltage characteristics of ferroelectric tunnel junctions, Phys. Rev. B **72**, 125341 (2005).
[29] D. Pantel and M. Alexe, Electroresistance effects in ferroelectric tunnel barriers, Phys. Rev. B **82**, 134105 (2010).
[30] Supriyo Datta, *Quantum Transport: Atom to Transistor* (Cambridge University Press, Cambridge, England, 2005).
[31] G. Gerra, A. K. Tagantsev, and N. Setter, Ferroelectricity in Asymmetric Metal-Ferroelectric-Metal Heterostructures: A Combined First-Principles–Phenomenological Approach, Phys. Rev. Lett. **98**, 207601 (2007).
[32] A. K. Tagantsev, G. Gerra, and N. Setter, Short-range and long-range contributions to the size effect in metal-ferroelectric-metal heterostructures, Phys. Rev. B **77**, 174111 (2008).
[33] Yang Liu, Xiaojie Lou, Manuel Bibes, and Brahim Dkhil, Effect of a built-in electric field in asymmetric ferroelectric tunnel junctions, Phys. Rev. B **88**, 024106 (2013).
[34] Yubo Qi and Andrew M. Rappe, Designing Ferroelectric Field-Effect Transistors Based on the Polarization-Rotation Effect for Low Operating Voltage and Fast Switching, Phys. Rev. Applied **4**, 044014 (2015).
[35] Javier Junquera and Philippe Ghosez, First-principles study of ferroelectric oxide epitaxial thin films and superlattices: Role of the mechanical and electrical boundary conditions, J. Comput. Theor. Nanosci. **5**, 2071 (2008).
[36] Eng-Kiang Tan, J. Osman, and D. R. Tilley, Theory of switching in bulk first-order ferroelectric materials, Phys. Status Solidi (b) **228**, 765 (2001).
[37] G. Vizdrik, S. Ducharme, V. M. Fridkin, and S. G. Yudin, Kinetics of ferroelectric switching in ultrathin films, Phys. Rev. B **68**, 094113 (2003).
[38] R. Kretschmer and K. Binder, Surface effects on phase transitions in ferroelectrics and dipolar magnets, Phys. Rev. B **20**, 1065 (1979).
[39] S. C. Chang, S. Manipatruni, D. Nikonov, and I. Young, Clocked domain wall logic using magnetoelectric effects, IEEE J. Explor. Solid-State Comput. Devices Circuits **2**, 1 (2016).
[40] S. L. Miller and P. J. McWhorter, Physics of the ferroelectric nonvolatile memory field effect transistor, J. Appl. Phys. **72**, 5999 (1992).
[41] R. Landauer, Spatial variation of currents and fields due to localized scatterers in metallic conduction, IBM J. Res. Dev. **1**, 223 (1957).
[42] Zhaohao Wang, Weisheng Zhao, Wang Kang, Anes Bouchenak-Khelladi, Yue Zhang, Youguang Zhang, Jacques-Olivier Klein, Dafin Ravelosona, and Claude Chappert, A physics-based compact model of ferroelectric tunnel junction for memory and logic design, J. Phys. D **47**, 045001 (2014).
[43] J. P. Velev, Chun-Gang Duan, K. D. Belashchenko, S. S. Jaswal, and E. Y. Tsymbal, Effect of Ferroelectricity on Electron Transport in $Pt/BaTiO_3/Pt$ Tunnel Junctions, Phys. Rev. Lett. **98**, 137201 (2007).
[44] Massimiliano Stengel, David Vanderbilt, and Nicola A. Spaldin, Enhancement of ferroelectricity at metal-oxide interfaces, Nat. Mater. **8**, 392 (2009).
[45] Martin Gajek, Manuel Bibes, Stephane Fusil, Karim Bouzehouane, Josep Fontcuberta, Agnes Barthelemy, and Albert Fert, Tunnel junctions with multiferroic barriers, Nat. Mater. **6**, 296 (2007).
[46] *Correlation Spectroscopy of Surfaces, Thin Films, and Nanostructures*, edited by Jrgen Kirschner and Jamal Berakdar (Wiley Online Library, New York, 2005).
[47] Charles Kittel, *Introduction to Solid State Physics*, 6th ed. (John Wiley & Sons, Inc., New York, 1986).
[48] Sou-Chi Chang, R. M. Iraei, S. Manipatruni, D. E. Nikonov, I. A. Young, and A. Naeemi, Design and analysis of copper and aluminum interconnects for all-spin logic, IEEE Trans. Electron Devices **61**, 2905 (2014).
[49] Sou-Chi Chang, S. Manipatruni, D. E. Nikonov, I. A. Young, and A. Naeemi, Design and analysis of Si interconnects for all-spin logic, IEEE Trans. Magn. **50**, 1 (2014).